

RKKY signatures as a probe of band properties and photoinduced topological phase transitions in MnBi_2Te_4 films

Ya-Xi Li,^{1,2} Rui-Qiang Wang,^{1,2} Ming-Xun Deng,^{1,2} Mou Yang,^{1,2} and Hou-Jian Duan^{1,2,*}

¹*Guangdong Basic Research Center of Excellence for Structure and Fundamental Interactions of Matter, Guangdong Provincial Key Laboratory of Quantum Engineering and Quantum Materials, School of Physics, South China Normal University, Guangzhou 510006, China*

²*Guangdong-Hong Kong Joint Laboratory of Quantum Matter, Frontier Research Institute for Physics, South China Normal University, Guangzhou 510006, China*

We present a systematic study of the Ruderman-Kittel-Kasuya-Yosida (RKKY) interaction in MnBi_2Te_4 films under both dark and illuminated conditions. In the dark, the intrinsic magnetism of MnBi_2Te_4 is shown to yield a stronger anisotropic RKKY spin model compared to nonmagnetic topological insulators, providing a clear signature for differentiating these systems. Furthermore, key band properties—such as energy gap, band degeneracy/splitting, and topological deformations of the Fermi surface—imprint distinct signatures on the RKKY interaction, enabling clear discrimination between even- and odd-septuple-layer (SL) films. This discrimination manifests in multiple ways: through the Fermi-energy dependence or spatial oscillations of the interaction for impurities on the same surface, or via the presence versus absence of spin-frustrated terms for those on different surfaces. Under off-resonant circularly polarized light, we track photoinduced topological phase transitions and identify two characteristic signatures at the phase boundary: a sign reversal in spin-frustrated terms and a dip in collinear RKKY components. These serve as fingerprints for circular-polarization-chirality-dependent topological transitions in even- and odd-SL films, respectively. Overall, this work establishes RKKY interactions as a sensitive magnetic probe for revealing both distinctive band properties and light-driven phase transitions in MnBi_2Te_4 films, thereby complementing conventional electrical measurements while providing new insights into the influence of intrinsic magnetism on the surface-state band structure.

I. INTRODUCTION

The interplay between nonmagnetic topological materials and magnetism enables the realization of novel topological phases, such as quantum anomalous Hall (QAH) insulators, axion insulators (AI), and Weyl semimetals [1–12]. These systems exhibit remarkable transport phenomena, including the dissipationless chiral edge states in QAH insulators [6–8], the quantized magnetoelectric effects in topological axion states [9–11], and the non-Abelian statistics of Majorana fermions [12]. Such unique properties render magnetic topological states highly promising for applications in spintronics and topological quantum computing. Conventionally, these states are achieved by incorporating magnetic dopants into host materials. A landmark in this approach was the prediction and subsequent observation of the QAH effect in Cr-doped $(\text{Bi},\text{Sb})_2\text{Te}_3$ thin films [7, 8, 13]. However, this method relies on extrinsic magnetism, making the resultant topological properties highly sensitive to the precise chemical composition and typically limited to very low temperatures [14]. These inherent drawbacks pose a formidable challenge for engineering diverse phases through doping, thus intensifying the search for a new class of intrinsic magnetic topological materials, where magnetism is an inherent property of the crystal lattice itself.

Among such intrinsic candidates, MnBi_2Te_4 has emerged as a canonical platform, attracting significant interest [15]. Its layered crystal structure, composed of septuple layers (SLs) with van der Waals bonding and an A-type antiferromagnetic

order, provides the foundation for unique quantum phenomena when confined to films. In the few-SL limit, a fundamental dichotomy arises: both the magnetic order and the resulting emergent topological states are governed entirely by the parity of the SL count [16–19]. Specifically, odd-SL films exhibit ferromagnetic (FM) order, characterized by parallel magnetization on their top and bottom surfaces. This FM configuration gives rise to the QAH state, identified by a Chern number $C = +1$ and a quantized Hall conductance e^2/h . In contrast, even-SL films maintain antiferromagnetic (AFM) order with antiparallel surface magnetizations, stabilizing the so-called AI state. The distinctive feature of this AI—setting it apart from a trivial insulator—is its quantized magnetoelectric coefficient $\theta = \pi$ [10, 20–22], even as it exhibits a zero Hall plateau ($C = 0$). Owing to this striking thickness dependence and intrinsic magnetism, MnBi_2Te_4 films stand as a highly promising platform for fundamental research and future device applications [19].

A key challenge in studying MnBi_2Te_4 films lies in the unambiguous identification of their distinct topological phases. This challenge is twofold. First, initial breakthroughs demonstrated the material's potential: the quantized QAH state was realized in an odd-SL film [23], and the AI state with a zero-Hall plateau was reported in an even-SL film [19], both at zero magnetic field. However, subsequent studies have revealed that electrical transport measurements alone are insufficient to reliably distinguish these states [24]. For instance, a nominal 5-SL (odd) device was found to exhibit vanishing Hall resistance and high longitudinal resistance—signatures previously associated with the even-SL AI state [19]—highlighting the ambiguity. This practical difficulty arises because the dissipationless edge current expected in an ideal QAH phase can be disrupted or shunted by various imperfections, allowing trans-

* dhjphd@163.com

port to become dominated by the insulating bulk or other dissipative channels [25]. Consequently, the characteristic transport signatures of a topological phase can be masked, making the sole reliance on resistivity and Hall measurements problematic for definitive phase identification. This ambiguity underscores the critical need for complementary, non-transport probes that can access the topological nature of the surface states. Second, beyond the intrinsic phases, MnBi_2Te_4 films enable access to a rich variety of photoninduced topological phases via circularly polarized light (CPL). As reported [26, 27], the resulting topological phase transitions depend not only on the SL count but also on the chirality of the light's circular polarization. This unique control mechanism raises a fundamental question: how can one reliably detect these complex, chirality-dependent phase transitions? Common approaches face obstacles (for instance, the Hall conductivity is easily compromised by bulk states when the energy gap is small; or direct detection of surface/edge states requires exceptionally clean surfaces), prompting the evaluation of new detection methods.

These two challenges motivate us to investigate the RKKY interaction as a versatile magnetic probe for the band properties of the topological surface states in MnBi_2Te_4 films. This proposal rests on two pillars. First, the RKKY interaction has proven to be a powerful tool for characterizing band structures and topological properties [28–49]. To utilize this capability, two magnetic impurities are placed on the film surface with a relatively large separation. The induced weak RKKY interaction between impurities leaves the host's band structure unperturbed [50], while its mediation by itinerant electrons makes it a sensitive probe of the system's band properties. Second, our investigation employs the low-energy model of MnBi_2Te_4 films established in Ref. [26], which effectively captures the distinct topological surface phases—namely, the QAH and AI phases—governed by intrinsic magnetism as described in Refs. [16–19]. By analyzing the behavior of the RKKY interaction in this model, we pursue two primary objectives: (i) to understand the modification of the surface-state band structure by intrinsic magnetism from a magnetic perspective, thereby extracting characteristic RKKY signatures that can distinguish between the nonmagnetic topological insulator, QAH (odd-SL), and AI (even-SL) phases, and thus address the experimental ambiguities outlined earlier. (ii) to track the evolution of topological phases under CPL by identifying the characteristic magnetic signatures linked to the polarization chirality. This dual approach provides a new perspective that complements conventional electrical measurements.

The paper is structured as follows. Sec. II presents the low-energy model for the surface states of MnBi_2Te_4 films, the rich topological phase transitions induced by CPL, and the method for calculating the RKKY interaction. Sec. III investigates three key aspects: (a) the influence of intrinsic magnetism on the RKKY spin model and the identification of signatures to distinguish MnBi_2Te_4 from nonmagnetic topological insulators; (b) the evolution of the collinear RKKY components with Fermi energy and its spatial oscillatory behavior, together with the characteristics of spin-frustrated terms, which serve

to differentiate between even- and odd-SL films; and (c) the variation of the RKKY amplitude with light parameters, enabling the extraction of magnetic signatures of polarization-chirality-dependent topological phase transitions. A summary is provided in Sec. IV.

II. MODELS AND METHOD

A. The effective model

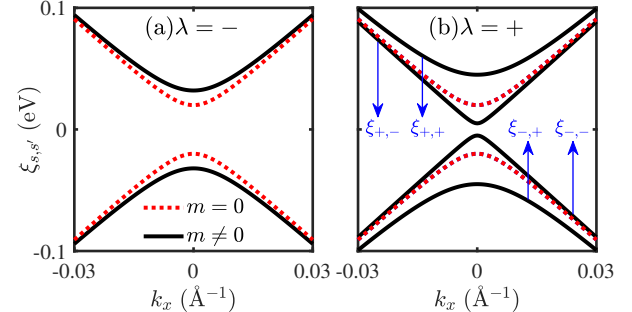


FIG. 1. k_x -axis dispersion for (a) even-SL ($\lambda = -$) and (b) odd-SL ($\lambda = +$) MnBi_2Te_4 films at different Zeeman coupling strengths ($m = 0, 0.025$ eV). Other parameters are $\Delta = 0.02$ eV and $v = 2.95$ eV \cdot \AA .

The effective Hamiltonian describing the surface states of MnBi_2Te_4 films—a model captured in Refs. [15–19] and formalized in Ref. [26]—is given by

$$H_0(\mathbf{k}) = \begin{pmatrix} h_{+,+}(\mathbf{k}) & \Delta\sigma_0 \\ \Delta\sigma_0 & h_{-,-}(\mathbf{k}) \end{pmatrix}. \quad (1)$$

This Hamiltonian effectively represents two coupled Dirac cones originating from the top and bottom surfaces of the film. In this expression, the Hamiltonian for an individual Dirac cone is given by $h_{s_i,\lambda}(\mathbf{k}) = s_i v(\mathbf{k} \times \boldsymbol{\sigma})_z + \lambda m \sigma_z$, where $s_i = \pm 1$ specifies the helicity of the Dirac cone, and $\lambda = \pm$ distinguishes between odd- ($\lambda = +$) and even-SL ($\lambda = -$) films. Here, $\boldsymbol{\sigma} = (\sigma_x, \sigma_y, \sigma_z)$ denotes the vector of Pauli matrices in spin space, with σ_0 representing the identity matrix. In this model, the parameters are defined as follows: v corresponds to the Fermi velocity, Δ quantifies the coupling between the two surface Dirac cones induced by finite-size effects, and m represents the strength of intrinsic magnetism, which arises from the Zeeman coupling associated with time-reversal-symmetry-breaking magnetic moments. When $m \neq 0$, the sign of λ —which is determined by the parity of the SL count—governs the selection between the AI phase ($\lambda = -$) and the QAH phase ($\lambda = +$). Finally, it is worth noting that the model reduces to that of a nonmagnetic topological insulator film for $m = 0$.

By diagonalizing the Hamiltonian in Eq. (1), we obtain the energy dispersion

$$\xi_{s,s'}(m, \lambda) = s \sqrt{m^2 + k^2 v^2 + \Delta^2 + s' \sqrt{2\Delta^2 m^2(1 + \lambda)}}, \quad (2)$$

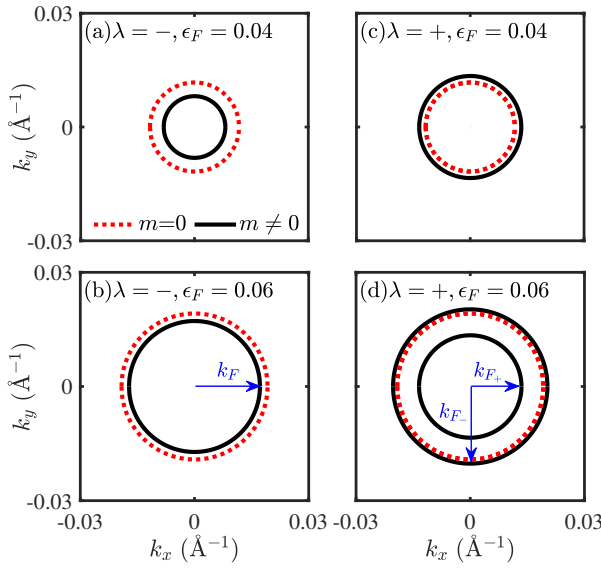


FIG. 2. Fermi surfaces of (a,b) even-SL ($\lambda = -$) and (c,d) odd-SL ($\lambda = +$) MnBi_2Te_4 thin films for different Zeeman coupling strengths $m = 0, 0.025$ eV. The Fermi energy is set to $\epsilon_F = 0.04$ eV in (a,c) and 0.06 eV in (b,d). Other parameters are identical to those in Fig. 1. Labels k_F and $k_{F\pm}$ in (b,d) denote the Fermi wave numbers for the even- and odd-SL films, respectively.

where $s = \pm$ labels the conduction-band and valence-band doublets, respectively, and $s' = \pm$ indexes the two subbands within either doublet. At $m = 0$, time-reversal (\mathcal{T}) symmetry ensures the degeneracy between the two subbands $\xi_{s,+}$ and $\xi_{s,-}$. The introduction of intrinsic magnetism ($m \neq 0$) in even-SL ($\lambda = -$) films breaks \mathcal{T} symmetry; however, the band degeneracy is still preserved by the combined symmetry of inversion (\mathcal{P}) and \mathcal{T} [25, 27]. In contrast to the $m = 0$ case, the bands experience a momentum-dependent shift: the conduction band moves upward while the valence band downward. This shift is most pronounced at $k_{x,y} = 0$, which enlarges the band gap from $\xi_g(m = 0) = 2\Delta$ to $\xi_g(m \neq 0, \lambda = -) = 2\sqrt{m^2 + \Delta^2}$, as illustrated in Fig. 1(a). Conversely, introducing magnetism ($m \neq 0$) in odd-SL ($\lambda = +$) films breaks \mathcal{PT} symmetry, which lifts the band degeneracy, resulting in split subbands where $\xi_{s,+} \neq \xi_{s,-}$, as depicted in Fig. 1(b). Examining the conduction band in detail, one subband, $\xi_{+,+}(m \neq 0, \lambda = +)$, rises above the original $\xi_{+,+}(m = 0)$ level (represented by the dashed line in Fig. 1(b)), while the other, $\xi_{+,-}(m \neq 0, \lambda = +)$, falls below it. Consequently, the band gap narrows to $\xi_g(m \neq 0, \lambda = +) = 2|m - \Delta|$.

In short, the introduction of m significantly modifies the band structure of both even- and odd-SL films, demonstrating a clear dependence on the SL count. This dependence is further reflected in distinct deformations of the Fermi surface. As shown in Figs. 2(a) and 2(b), the Fermi surface in even-SL ($\lambda = -$) films remains a single circle for different Fermi energies. This circle is an enlarged version of the $m = 0$ case, and the degree of enlargement decreases as the Fermi energy increases. Thus, varying the Fermi energy does not alter the topology of the Fermi surface. In contrast, for odd-SL ($\lambda = +$)

films, varying the Fermi energy drives a topological deformation of the Fermi surface, i.e., a Lifshitz transition [Figs. 2(c) and 2(d)]. Specifically, at low Fermi energies, the Fermi surface is a single circle [Fig. 2(c)], while at higher energies it consists of two concentric circles [Fig. 2(d)]—one contracted and the other expanded relative to the original $m = 0$ circular Fermi surface. This transition originates entirely from the unique band splitting shown in Fig. 1(b) and represents a key band characteristic that distinguishes QAH insulators from both AI and nonmagnetic topological insulators.

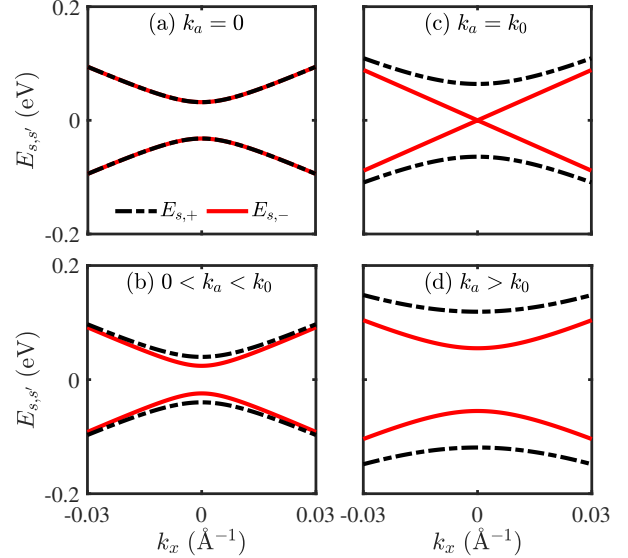


FIG. 3. Evolution of the k_x -axis dispersion for even-SL ($\lambda = -$) MnBi_2Te_4 films at different light parameter k_a : (a) $k_a = 0$, (b) $k_a < k_0$ (where $k_0 = \sqrt{\hbar^2\omega^2(m^2 + \Delta^2)/v}$; here $k_a = 0.03$ \AA^{-1}), (c) $k_a = k_0$, and (d) $k_a > k_0$ ($k_a = 0.1$ \AA^{-1}). Results are shown for right-handed ($\eta = +$) CPL; identical dispersion is obtained for left-handed ($\eta = -$) polarization.

Under irradiation by CPL, MnBi_2Te_4 films exhibit a rich variety of topological phase transitions, as documented in Refs. [26, 27]. In contrast to conventional photoinduced topological transitions, these phases depend critically on both the chirality of the circular polarization and the number of SL. To systematically track how the energy bands and topological indices evolve with the parameters of the light, we compute the effective Hamiltonian under illumination. We begin by assuming normal incidence of CPL on the film surface. The time-dependent Hamiltonian is obtained via Peierls substitution: $\mathbf{k} \rightarrow \mathbf{k} + e\mathbf{A}/\hbar$, with the vector potential $\mathbf{A}(t) = A_0[0, \cos(\Omega t), \eta \sin(\Omega t)]$ and period $T = 2\pi/\Omega$. Here, $\eta = +$ (or $-$) denotes right-handed (or left-handed) polarization, and A_0 is the amplitude of the vector potential. Applying Floquet theory [51–53] under the off-resonant condition $\hbar\Omega \gg BW$ (with $\hbar\omega = 1$ eV and the bandwidth $BW = 0.2$ eV), the photoinduced correction to the Hamiltonian takes the form

$$H(\mathbf{k}) = V_0 + \sum_{n \geq 1} \frac{[V_{+n}, V_{-n}]}{n\hbar\Omega} + O\left(\frac{1}{\Omega^2}\right), \quad (3)$$

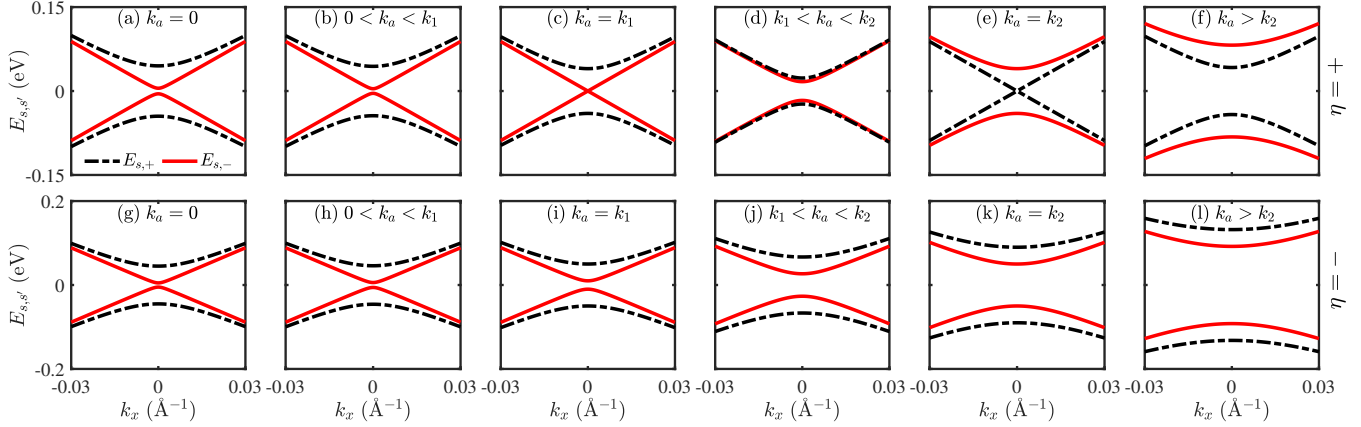


FIG. 4. k_x -axis dispersion for odd-SL ($\lambda = +$) MnBi_2Te_4 films at different light parameter k_a (where $k_1 = \sqrt{\hbar\omega(m - \Delta)}/v$ and $k_2 = \sqrt{\hbar\omega(m + \Delta)}/v$): (a,g) $k_a = 0$, (b,h) $k_a < k_1$ ($k_a = 0.01 \text{ \AA}^{-1}$), (c,i) $k_a = k_1$, (d,j) $k_1 < k_a < k_2$ ($k_a = 0.05 \text{ \AA}^{-1}$), (e,k) $k_a = k_2$, and (f,l) $k_a > k_2$ ($k_a = 0.1 \text{ \AA}^{-1}$). The top row (a-f) and bottom row (g-l) correspond to right- ($\eta = +$) and left-handed ($\eta = -$) CPL, respectively.

where $V_n = \frac{1}{T} \int_0^T H_0(\mathbf{k} + e\mathbf{A}/\hbar) e^{-in\hbar\Omega t} dt$. After some algebraic calculations, V_n can be solved as

$$V_0 = H_0(\mathbf{k}),$$

$$V_{+1} = \frac{vk_a}{2} \begin{pmatrix} \sigma_y - i\eta\sigma_x & 0 \\ 0 & -\sigma_y + i\eta\sigma_x \end{pmatrix}, \quad (4)$$

where $k_a = eA_0/\hbar$. Other Floquet sidebands follow as $V_{-1} = V_{+1}^\dagger$ and $V_n = 0$ for $n \geq 2$. Substituting these results into Eq. (3) yields the effective Hamiltonian

$$H(\mathbf{k}) = H_0(\mathbf{k}) - \eta m_\omega \sigma_z, \quad (5)$$

where $m_\omega = v^2 k_a^2 / (\hbar\omega)$.

The diagonalization of $H(\mathbf{k})$ in Eq. (5) leads to the photon-dressed energy dispersion:

$$E_{s,s'}(\lambda = -) = s \sqrt{k^2 v^2 + (m_\omega + s' \sqrt{\Delta^2 + m^2})^2}, \quad (6)$$

$$E_{s,s'}(\lambda = +) = s \sqrt{k^2 v^2 + [\Delta + s' (m - \eta m_\omega)]^2}.$$

Based on Eqs. (6), we plot the energy bands for various values of k_a in Figs. 3 and 4 to track the evolution of the dispersion. For even-SL ($\lambda = -$) films, as k_a increases from zero, the surface-state bands undergo a gap closing and reopening at $k_a = k_0$ ($k_0 = \sqrt[4]{\hbar^2 \omega^2 (m^2 + \Delta^2)}/v$), as shown in Fig. 3. This evolution is independent of the chirality of the circular polarization, resulting in identical bands for both $\eta = +$ and $\eta = -$. In contrast, the response of odd-SL ($\lambda = +$) films depends strongly on the polarization chirality. Specifically, for right-handed polarization ($\eta = +$), increasing k_a induces successive gap closings and reopenings at $k_a = k_1$ and $k_a = k_2$, with $k_1 = \sqrt{\hbar\omega(m - \Delta)}/v$ and $k_2 = \sqrt{\hbar\omega(m + \Delta)}/v$. The first gap closing at k_1 is dominated by the $E_{s,-}$ band (red solid lines in Fig. 4(c)), whereas the second at k_2 is dominated by the $E_{s,+}$ band (black dashed lines in Fig. 4(e)). For left-handed polarization ($\eta = -$), however, increasing k_a monotonically

enlarges the gap without any closing or reopening. Since a gap closing and reopening can potentially induce a topological phase transition, we thus expect rich topological transitions in even-SL ($\lambda = -$) films, as well as in odd-SL ($\lambda = +$) films under right-handed polarization.

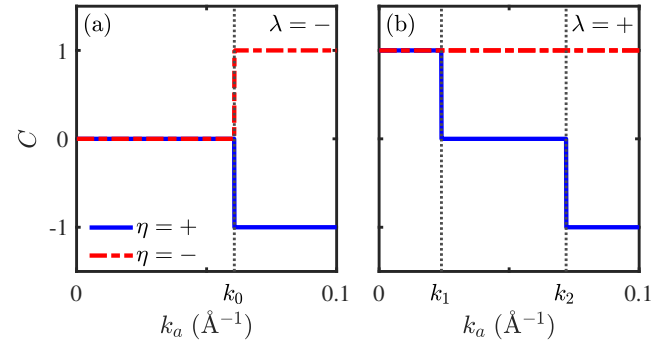


FIG. 5. Chern number vs. light parameter k_a for (a) even-SL ($\lambda = -$) and (b) odd-SL ($\lambda = +$) MnBi_2Te_4 films under both right- ($\eta = +$) and left-handed ($\eta = -$) CPL. Parameters: $m = 0.025 \text{ eV}$; others as in Fig. 1.

To further clarify and confirm the topological phase transitions in MnBi_2Te_4 films under CPL, we evaluate the Chern number C , which is defined as

$$C = \frac{1}{2\pi} \sum_n \int_{BZ} dk \Omega_{xy}^n, \quad (7)$$

where the Berry curvature Ω_{xy}^n for the n th band is expressed as [54]

$$\Omega_{xy}^n(\mathbf{k}) = i \sum_{m \neq n} \frac{\left\langle u_n \left| \frac{\partial H}{\partial k_x} \right| u_m \right\rangle \left\langle u_m \left| \frac{\partial H}{\partial k_y} \right| u_n \right\rangle - (x \leftrightarrow y)}{(E_n - E_m)^2}. \quad (8)$$

Here, m is a band index, while E_n and $|u_n\rangle$ denote the eigenvalue and eigenstate of the n -th band, respectively. We set the Fermi energy to zero so that the Chern number C sums over all occupied valence bands, which correspond to the two valence subbands shown in Figs. 3 and 4. Substituting Eq. (8) into Eq. (7) and performing the integration, we arrive at the following explicit results:

$$C(\lambda = -) = \frac{\operatorname{sgn}(\sqrt{\Delta^2 + m^2} + \eta m_\omega) - \operatorname{sgn}(\sqrt{\Delta^2 + m^2} - \eta m_\omega)}{2}, \quad (9)$$

$$C(\lambda = +) = \frac{\operatorname{sgn}(m + \eta m_\omega + \Delta) + \operatorname{sgn}(m + \eta m_\omega - \Delta)}{2}.$$

Using Eq. (9), we trace the evolution of the Chern number with the light parameter k_a , as shown in Fig. 5. In the even-SL ($\lambda = -$) case [Fig. 5(a)], once k_a exceeds the critical value k_0 , the system transitions from the original AI phase ($C = 0$) into a QAH phase. The Chern number of this resulting QAH phase depends on the polarization chirality: it takes $C = -1$ for $\eta = +$ and $C = 1$ for $\eta = -$. For the odd-SL ($\lambda = +$) films under right-handed polarization ($\eta = +$), the system undergoes two phase transitions as k_a increases. As illustrated in Fig. 5(b), it evolves successively from a QAH phase ($C = +1$) to a normal insulator (NI) phase ($C = 0$), and finally to another QAH phase ($C = -1$). The transition points occur precisely at $k_a = k_1$ and $k_a = k_2$, which correspond to the gap-closing cases shown in Figs. 4(c) and 4(e), respectively. In contrast, under left-handed polarization ($\eta = -$), the system remains in the QAH phase for all k_a , as no gap closure and reopening occurs (see Fig. 4). These findings are fully consistent with the results reported in Ref. [26]. Building on this optically controllable platform, we next aim to extract signatures from the RKKY interaction to probe these chirality-dependent, photoninduced topological phase transitions.

B. The RKKY interaction

We model the RKKY interaction in a MnBi_2Te_4 film by considering two magnetic impurities placed on its surfaces, located at positions \mathbf{r}_i and \mathbf{r}_j , respectively. The total Hamiltonian of the system, which includes the spin-exchange interaction between the impurities and the host electrons within the s - d model, is given by

$$H' = H + H_{\text{int}}, \quad (10)$$

$$= H - J_c \mathbf{S}_i \cdot \mathbf{s}_i - J_c \mathbf{S}_j \cdot \mathbf{s}_j,$$

where J_c denotes the strength of the exchange coupling, \mathbf{S}_i represents the spin of the impurity at site \mathbf{r}_i , and $\mathbf{s}_i = \frac{1}{2} c_{ia}^\dagger \boldsymbol{\sigma}_{ab} c_{ib}$ is the spin of the host electrons at the same site. Since the two impurities couple indirectly via the itinerant electrons, the resulting effective exchange interaction between them is the RKKY interaction. In the weak-coupling limit where J_c is sufficiently small, H_{int} can be treated as a perturbation. Applying standard second-order perturbation theory [55–58] in J_c , the explicit form of this RKKY interaction is

derived as:

$$H_R^{\alpha\beta} = -\frac{J_c^2}{\pi} \operatorname{Im} \int_{-\infty}^{\epsilon_F} d\epsilon \operatorname{Tr} [(\mathbf{S}_1 \cdot \boldsymbol{\sigma}) G_{\alpha\beta}(\mathbf{R}, \epsilon) (\mathbf{S}_2 \cdot \boldsymbol{\sigma}) G_{\beta\alpha}(-\mathbf{R}, \epsilon)], \quad (11)$$

where $\mathbf{R} = \mathbf{r}_i - \mathbf{r}_j$, ϵ_F is the Fermi energy, and $G_{\alpha\beta}(\pm\mathbf{R}, \epsilon)$ denotes a matrix element of the retarded Green's function $G(\pm\mathbf{R}, \epsilon)$ associated with the unperturbed Hamiltonian H in real space. The subscripts $\alpha, \beta \in t, b$ indicate whether an impurity is located on the top (t) or bottom (b) surface of the film.

The calculation of the RKKY interaction requires the real-space retarded Green's function. Starting from the Hamiltonian $H(\mathbf{k})$ given in Eq. (5), we express the Green's function $G(\pm\mathbf{R}, \epsilon)$ in Lehmann's representation as

$$G(\pm\mathbf{R}, \epsilon) = \frac{1}{(2\pi)^2} \int e^{\pm i\mathbf{k} \cdot \mathbf{R}} \frac{1}{\epsilon + i0^+ - H(\mathbf{k})} d^2\mathbf{k}. \quad (12)$$

Because $H(\mathbf{k})$ acts on a space that combines the degrees of freedom from both the top and bottom surfaces, the Green's function takes the following block-matrix form:

$$G(\pm\mathbf{R}, \epsilon) = \begin{pmatrix} G_{tt}(\pm\mathbf{R}, \epsilon) & G_{tb}(\pm\mathbf{R}, \epsilon) \\ G_{bt}(\pm\mathbf{R}, \epsilon) & G_{bb}(\pm\mathbf{R}, \epsilon) \end{pmatrix}, \quad (13)$$

where the subscript t (b) indicates that the impurity is located on the top (bottom) surface of the film.

In this work, we consider two distinct impurity configurations: both impurities on the same surface, and one impurity on the top surface with the other on the bottom. We begin by examining the former scenario and, for convenience, assume that both impurities reside on the top surface. In this case, substituting $H(\mathbf{k})$ from Eq. (5) into Eq. (12) and performing algebraic manipulations yields $G_{tt}(\pm\mathbf{R}, \epsilon)$ in the form

$$G_{tt}(\pm\mathbf{R}, \epsilon) = \begin{pmatrix} f_0 + f_z & \pm e^{-i\theta_R} f \\ \mp e^{i\theta_R} f & f_0 - f_z \end{pmatrix}. \quad (14)$$

The matrix elements (f_0, f_z, f) of $G_{tt}(\pm\mathbf{R}, \epsilon)$ depend on the SL

count via λ and are given explicitly by

$$\begin{aligned}
f_0(\lambda = -) &= -\sum_{s'=\pm} \frac{\epsilon(\gamma + s'\eta mm_\omega)K_0\left(R/\sqrt{\frac{v^2}{\zeta_{-,s'}^2 - \epsilon^2}}\right)}{\gamma/\alpha}, \\
f_z(\lambda = -) &= -\sum_{s'=\pm} \frac{\alpha\left[(m + \eta m_\omega)(\gamma + s'\eta mm_\omega) + s'\eta m_\omega\Delta^2\right]}{\gamma/K_0\left(R/\sqrt{\frac{v^2}{\zeta_{-,s'}^2 - \epsilon^2}}\right)}, \\
f(\lambda = -) &= -\frac{\alpha}{\gamma} \sum_{s'=\pm} \frac{(\gamma + s'\eta mm_\omega)}{\sqrt{\zeta_{-,s'}^2 - \epsilon^2}} K_1\left(R/\sqrt{\frac{v^2}{\zeta_{-,s'}^2 - \epsilon^2}}\right), \\
f_0(\lambda = +) &= -\alpha\epsilon \sum_{s'=\pm} K_0\left(R/\sqrt{\frac{v^2}{\zeta_{+,s'}^2 - \epsilon^2}}\right), \\
f_z(\lambda = +) &= -\alpha \sum_{s'=\pm} \zeta_{+,s'} K_0\left(R/\sqrt{\frac{v^2}{\zeta_{+,s'}^2 - \epsilon^2}}\right), \\
f(\lambda = +) &= -\alpha \sum_{s'=\pm} \frac{1}{\sqrt{\frac{1}{\zeta_{+,s'}^2 - \epsilon^2}}} K_0\left(R/\sqrt{\frac{v^2}{\zeta_{+,s'}^2 - \epsilon^2}}\right),
\end{aligned} \tag{15}$$

where $\alpha = 1/4\pi v^2$, $\gamma = m_\omega \sqrt{\Delta^2 + m^2}$, $\zeta_{+,s'} = m + \eta m_\omega + s'\Delta$, $\zeta_{-,s'} = |m_\omega + s' \sqrt{\Delta^2 + m^2}|$ and $K_n(x)$ ($n = 0, 1$) denotes the n th-order modified Bessel function of the second kind.

By substituting $G_{tt}(\pm\mathbf{R}, \epsilon)$ from Eq. (14) into Eq. (11) and tracing over the spin degrees of freedom, the RKKY interaction H_R^{tt} can be expressed in the following form:

$$H_R^{tt}(\lambda) = \sum_i J_{ii}(\lambda) S_1^i S_2^i + J_f^z(\lambda) (S_1^x S_2^y + S_1^y S_2^x) + J_{DM}(\lambda) \bar{\mathbf{e}}_R \cdot (\mathbf{S}_1 \times \mathbf{S}_2), \tag{16}$$

with

$$\begin{aligned}
J_{xx}(\lambda) &= -\frac{2J_c^2}{\pi} \text{Im} \int_{-\infty}^{\epsilon_F} [f_0^2 - f_z^2 - f^2 \cos(2\theta_R)] d\epsilon, \\
J_{yy}(\lambda) &= -\frac{2J_c^2}{\pi} \text{Im} \int_{-\infty}^{\epsilon_F} [f_0^2 - f_z^2 + f^2 \cos(2\theta_R)] d\epsilon, \\
J_{zz}(\lambda) &= -\frac{2J_c^2}{\pi} \text{Im} \int_{-\infty}^{\epsilon_F} [f_0^2 + f_z^2 - f^2] d\epsilon, \\
J_f^z(\lambda) &= -\frac{2J_c^2}{\pi} \text{Im} \int_{-\infty}^{\epsilon_F} [-f^2 \sin(2\theta_R)] d\epsilon, \\
J_{DM}(\lambda) &= -\frac{4J_c^2}{\pi} \text{Im} \int_{-\infty}^{\epsilon_F} (f_0 f) d\epsilon
\end{aligned} \tag{17}$$

where $\bar{\mathbf{e}}_R = (-\sin \theta_R, \cos \theta_R, 0)$. In Eq. (16), J_{ii} couples collinear spins, J_f^z represents the spin-frustrated term, and J_{DM} corresponds to the Dzyaloshinskii-Moriya (DM) interaction.

For the configuration where the two impurities are placed on the top and bottom surfaces respectively, the corresponding

Green's function $G_{bt}(\mathbf{R}, \epsilon)$ takes the form

$$G_{bt}(\mathbf{R}, \epsilon) = \begin{pmatrix} g_0 + g_z & e^{-i\theta_R} g \\ \lambda e^{i\theta_R} g & g_0 - g_z \end{pmatrix}, \tag{18}$$

where g_0 , g_z , and g are functions of λ , given explicitly by

$$\begin{aligned}
g_0(\lambda = -) &= -\frac{\alpha\Delta v^2/\hbar\omega}{\sqrt{\Delta^2 + m^2}} \sum_{s'=\pm} (k_0^2 + s'k_a^2) K_0\left(R/\sqrt{\frac{v^2}{\zeta_{-,s'}^2 - \epsilon^2}}\right), \\
g_z(\lambda = -) &= -\frac{\alpha}{\gamma} \eta \Delta m_\omega \epsilon \sum_{s'=\pm} s' K_0\left(R/\sqrt{\frac{v^2}{\zeta_{-,s'}^2 - \epsilon^2}}\right), \\
g(\lambda = -) &= \frac{\alpha}{\gamma} \eta \Delta m_\omega \sum_{s'=\pm} \frac{s' K_1\left(R/\sqrt{\frac{v^2}{\zeta_{-,s'}^2 - \epsilon^2}}\right)}{\sqrt{\frac{1}{\zeta_{-,s'}^2 - \epsilon^2}}}, \\
g_0(\lambda = +) &= -\alpha \sum_{s'=\pm} s' \zeta_{+,s'} K_0\left(R/\sqrt{\frac{v^2}{\zeta_{+,s'}^2 - \epsilon^2}}\right), \\
g_z(\lambda = +) &= -\alpha \epsilon \sum_{s'=\pm} s' K_0\left(R/\sqrt{\frac{v^2}{\zeta_{+,s'}^2 - \epsilon^2}}\right), \\
g(\lambda = +) &= -\alpha \sum_{s'=\pm} \frac{s' K_1\left(R/\sqrt{\frac{v^2}{\zeta_{+,s'}^2 - \epsilon^2}}\right)}{\sqrt{\frac{1}{\zeta_{+,s'}^2 - \epsilon^2}}}.
\end{aligned} \tag{19}$$

Following the same procedure as for H_R^{tt} , we obtain the RKKY interaction H_R^{tb}

$$H_R^{tb}(\lambda) = \sum_i \mathcal{J}_{ii}(\lambda) S_1^i S_2^i + \sum_{i=x,y,z} \mathcal{J}_f^i(\lambda) (S_1^j S_2^k + S_1^k S_2^j), \tag{20}$$

where (j, k) form an even permutation of the Levi-Civita symbol for a fixed i . Unlike H_R^{tt} in Eq. (16), H_R^{tb} lacks the DM interaction but contains two additional spin-frustrated terms, \mathcal{J}_f^x and \mathcal{J}_f^y . Their explicit expressions, together with the other components, are

$$\begin{aligned}
\mathcal{J}_{xx}(\lambda) &= -\frac{2J_c^2}{\pi} \text{Im} \int_{-\infty}^{\epsilon_F} [g_0^2 - g_z^2 + g^2 \cos(2\theta_R)] d\epsilon, \\
\mathcal{J}_{yy}(\lambda) &= -\frac{2J_c^2}{\pi} \text{Im} \int_{-\infty}^{\epsilon_F} [g_0^2 - g_z^2 - g^2 \cos(2\theta_R)] d\epsilon, \\
\mathcal{J}_{zz}(\lambda) &= -\frac{2J_c^2}{\pi} \text{Im} \int_{-\infty}^{\epsilon_F} [g_0^2 + g_z^2 - g^2] d\epsilon, \\
\mathcal{J}_f^x(\lambda) &= -\frac{4J_c^2}{\pi} \text{Im} \int_{-\infty}^{\epsilon_F} [\theta(\lambda)g_z + \theta(-\lambda)g_0] g \sin \theta_R d\epsilon, \\
\mathcal{J}_f^y(\lambda) &= -\frac{4J_c^2}{\pi} \text{Im} \int_{-\infty}^{\epsilon_F} [\theta(\lambda)g_z + \theta(-\lambda)g_0] g \cos \theta_R d\epsilon, \\
\mathcal{J}_f^z(\lambda) &= -\frac{2J_c^2}{\pi} \text{Im} \int_{-\infty}^{\epsilon_F} [g^2 \sin(2\theta_R)] d\epsilon,
\end{aligned} \tag{21}$$

where $\theta(\lambda)$ denotes the Heaviside step function.

III. RESULTS AND DISCUSSIONS

This section is structured into three parts. In the first two parts, we focus on the RKKY interactions in the absence of light. Specifically, the first part presents the magnetic signatures that distinguish MnBi_2Te_4 films ($m \neq 0$) from nonmagnetic topological insulator films ($m = 0$). The second part identifies the magnetic signals that differentiate even-SL (AI) and odd-SL (QAH insulators) MnBi_2Te_4 films. In the final part, we analyze RKKY interactions under off-resonant CPL. Here, we aim to derive magnetic signals that probe topological phase transitions dependent on both the circular polarization chirality η and the SL count λ .

A. Distinguishing MnBi_2Te_4 ($m \neq 0$) and nonmagnetic topological insulator ($m = 0$)

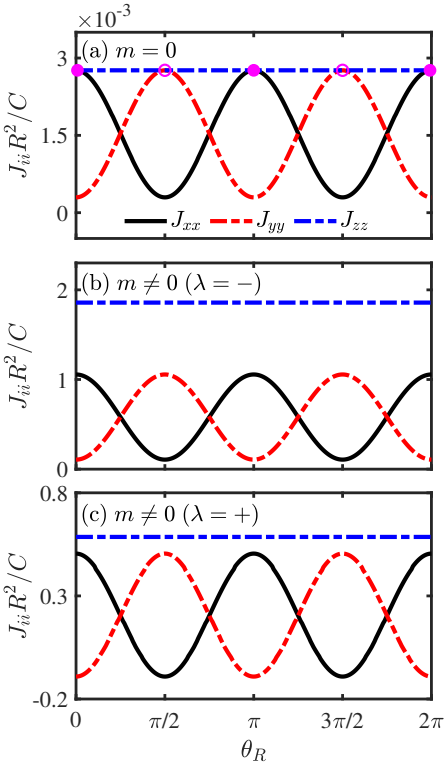


FIG. 6. Dependence of the collinear RKKY components J_{ii} on the azimuthal angle θ_R of the impurities, with impurities placed on the same surface. Results are presented for (a) $m = 0$, (b) $m = 0.025$ eV with $\lambda = -$ (even-SL films), and (c) $m = 0.025$ eV with $\lambda = +$ (odd-SL films). Other parameters are $\epsilon_F = 0.04$ eV, $\Delta = 0.02$ eV, $v = 2.95$ eV·Å, $a = \Delta/v$, and $Ra = 10$.

We begin by examining the collinear RKKY components J_{ii} , as they are particularly sensitive to the presence of finite m . For impurities deposited on the same surface with a fixed separation R , the dependence of J_{ii} on the azimuthal angle $\theta_R = \arctan(R_y/R_x)$ is computed using Eqs. (15) and (17), as

summarized in Fig. 6. In the case of $m = 0$, the results in Fig. 6(a) align with previous work [59]. In particular, when impurities are positioned along the axial directions $\theta_R = n\pi/2$ ($n = 0, 1, 2, 3$), the components J_{ii} satisfy $J_{zz} = J_{xx} \neq J_{yy}$ (solid circles in Fig. 6(a)) or $J_{zz} = J_{yy} \neq J_{xx}$ (open circles), corresponding to XYX -type and XYY -type RKKY spin models, respectively. It is noteworthy that both models exhibit a moderate anisotropy, governed primarily by the f^2 term in Eq. (17).

In contrast, under a finite m , both even-SL ($\lambda = -$ in Fig. 6(b)) and odd-SL ($\lambda = +$ in Fig. 6(c)) MnBi_2Te_4 films display the same qualitative behavior: the original XYX -type (at $\theta_R = 0, \pi$) or XYY -type (at $\theta_R = \pi/2, 3\pi/2$) model transforms into an XYZ -type model, characterized by $J_{xx} \neq J_{zz} \neq J_{yy}$. This XYZ spin model exhibits the strongest anisotropy—a stark contrast to the moderate anisotropy found at $m = 0$. The emergence of such extreme anisotropy is entirely due to the finite m (i.e., intrinsic magnetism), which introduces an additional correction to J_{ii} via the f_z^2 term in Eq. (17). Notably, the spin model originating purely from f_z^2 is of XXZ -type, distinct from the f^2 -induced XYX - or XYY -type models. Thus, the presence of finite m leads to a hybrid of XXZ and XYX (or XYY), resulting in the common XYZ -type spin model seen in both Fig. 6(b) and (c).

Taken together, these findings confirm that the RKKY spin model establishes a clear diagnostic criterion, i.e., the marked anisotropy contrast of this spin model between the magnetic ($m \neq 0$) and non-magnetic ($m = 0$) cases, for determining the introduction of intrinsic magnetism. Thus, it robustly distinguishes MnBi_2Te_4 ($m \neq 0$) from nonmagnetic topological insulators ($m = 0$).

B. Differentiating even-SL ($\lambda = -$) and odd-SL ($\lambda = +$) MnBi_2Te_4 films

The preceding discussion reveals a key limitation: within the $m \neq 0$ framework, the spin model exhibits universality across even- ($\lambda = -$) and odd-SL ($\lambda = +$) MnBi_2Te_4 films, and fails to effectively differentiate between them, as evidenced by the identical XYZ -type spin model in Fig. 6(b,c). This limitation originates from the inability of the spin model to capture the detailed band properties of MnBi_2Te_4 films shown in Figs. 1 and 2. To distinguish between even- ($\lambda = -$) and odd-SL ($\lambda = +$) MnBi_2Te_4 films, one must turn to magnetic signals that are sensitive to these band properties.

1. Characteristic Kinks: ϵ_F -Dependent RKKY Interaction

An effective approach is to investigate the evolution of J_{zz} with the Fermi energy ϵ_F , as shown in Fig. 7. In both cases ($\lambda = \pm$), a primary kink is observed at $\epsilon_c = \xi_g(\lambda)/2$, where $\xi_g(\lambda)$ is the band gap for the even- ($\lambda = -$) and odd-SL ($\lambda = +$) films in Fig. 1. This kink arises because the Fermi energy ϵ_F crosses the band edge: when $\epsilon_F < \epsilon_c$, it lies within the band gap, suppressing J_{zz} ; when $\epsilon_F > \epsilon_c$, electrons from the conduction band activate the interaction, causing J_{zz} to rise

abruptly. Thus, this kink serves as a universal signature of the band gap $\xi_g(\lambda)$.

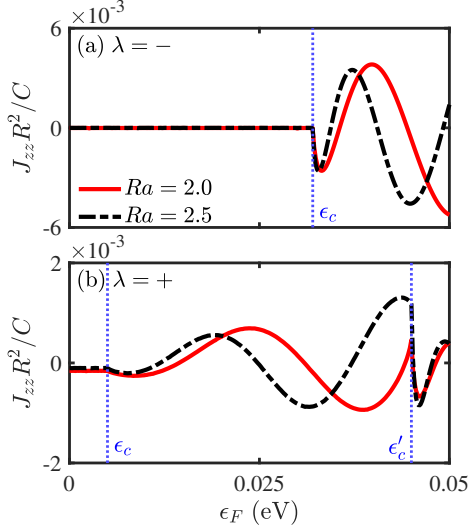


FIG. 7. The RKKY component J_{zz} as a function of the Fermi energy ϵ_F , with impurities placed on the same surface. Results are presented for (a) even-SL ($\lambda = -$) and (b) odd-SL ($\lambda = +$) films with different impurity distances ($Ra = 2.0, 2.5$). Other parameters are $\Delta = 0.02$ eV, $v = 2.95$ eV·Å, $a = \Delta/v$ and $\theta_R = \pi/4$.

The critical distinction, however, emerges for the $\lambda = +$ case, where a second, distinctive kink is observed at a higher energy $\epsilon'_c = \xi'_g(\lambda = +)/2$, as seen in Fig. 7(b). This kink is determined by the gap $\xi'_g(\lambda = +)$ between the bands $\xi_{+,+}$ and $\xi_{-,+}$ in Fig. 1(b). Its physical origin lies in the unique band splitting of the $\lambda = +$ case. Mechanistically, when $\epsilon_F < \epsilon'_c$, the magnetic interaction originates only from the ξ_{+-} band. Once ϵ_F surpasses ϵ'_c , electrons from the split band $\xi_{+,+}$ begin to contribute, causing a sudden change in J_{zz} that manifests as the kink. This second kink, directly linked to the SL-specific band splitting, therefore provides a definitive magnetic signature for distinguishing odd-SL ($\lambda = +$) films from their even-SL ($\lambda = -$) counterparts. Furthermore, this signal is robust, as the kink positions are independent of the impurity distance R (as shown in Fig. 7) and are also observable in other RKKY components (not shown here).

2. Distinct Oscillation Patterns

Alternatively, the even- ($\lambda = -$) and odd-SL ($\lambda = +$) MnBi_2Te_4 films can also be distinguished by investigating the oscillatory behavior of J_{zz} as a function of the impurity distance R . As shown in Fig. 8(a), for the $\lambda = -$ case, J_{zz} always exhibits a single-period oscillation, regardless of the Fermi energy ϵ_F . This behavior is dictated by the Fermi surface of the even-SL films. As depicted in Fig. 2(a, b), their Fermi surface consistently consists of a single contour. This means that changing ϵ_F only alters the size of this contour without changing its topological nature. Consequently, a single Fermi contour has a single radius and thus corresponds to a single

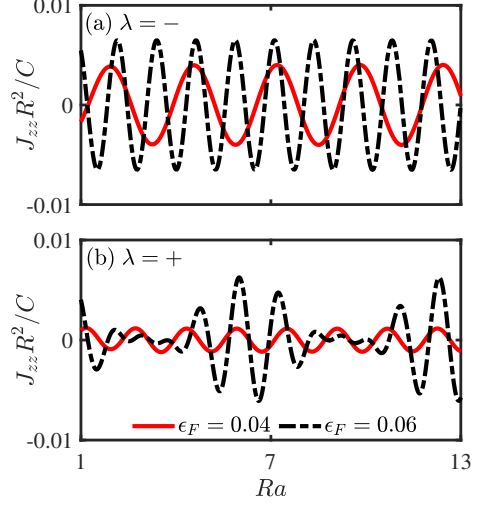


FIG. 8. The R -dependent RKKY component J_{zz} for (a) even-SL ($\lambda = -$) and (b) odd-SL ($\lambda = +$) films, with impurities placed on the same surface. Different Fermi energies ($\epsilon_F = 0.04, 0.06$ eV) are considered, and other parameters are identical to those in Fig. 7.

Fermi wave number k_F (Fig. 2(b)), which in turn directly dictates a single oscillation period ($T = \pi/k_F$) for the interaction [60–62].

In contrast, for the $\lambda = +$ (odd-SL) case, J_{zz} maintains a single-period oscillation at lower Fermi energies but develops a double-period oscillation at larger values, as shown in Fig. 8(b). The emergence of this double-period oscillation stems from the peculiar Fermi surface of odd-SL films at large Fermi energies, which comprises two separated concentric contours (Fig. 2(d)). Their distinct radii correspond to two different Fermi wave numbers, k_{F_-} and k_{F_+} in Fig. 2(d), which naturally provide two distinct oscillation periods (π/k_{F_-} and π/k_{F_+}) for the magnetic interaction. This transition from single- to double-period oscillation precisely reflects a topological deformation of the Fermi surface—known as a Lifshitz transition—in the odd-SL films. Hence, by tracing the evolution of the oscillation pattern with different ϵ_F , one can effectively distinguish between the even- ($\lambda = -$) and odd-SL ($\lambda = +$) films.

3. Presence/Absence of Spin-Frustrated Terms

All magnetic signals discussed previously were obtained with impurities placed on the same surface. In contrast, placing impurities on different surfaces yields distinct magnetic signals, which can also distinguish between even-SL ($\lambda = -$) and odd-SL ($\lambda = +$) films. Due to the vanishing of $g_z(\lambda = -)$ and $g(\lambda = -)$ in Eq. (19) in the absence of CPL, the RKKY interaction H_R^{tb} for the even-SL ($\lambda = -$) case, given in Eq. (20), simplifies to

$$H_R^{tb}(\lambda = -) = \mathcal{J}_H \mathbf{S}_1 \cdot \mathbf{S}_2, \quad (22)$$

where \mathcal{J}_H originates exclusively from $g_0(\lambda = -)$. The above equation indicates that the interaction here is purely collinear, consisting solely of a Heisenberg term.

For the $\lambda = +$ case, however, the RKKY interaction retains the general form of Eq. (20). It therefore includes not only collinear RKKY components but also three additional types of spin-frustrated terms (non-collinear components) $\mathcal{J}_f^{x,y,z}$, which are always absent in the $\lambda = -$ case [Eq. (22)]. The emergence of these additional terms is directly attributable to the band splitting in odd-SL ($\lambda = +$) films. This splitting forces $g(\lambda = +)$ in Eq. (19) to be non-zero, which, according to Eq. (21), is the necessary condition for generating the spin-frustrated terms. The non-zero nature of $g(\lambda = +)$ can be understood from its explicit form: $g(\lambda = +) \propto \sum_{s'} s' K_0(x_{s'})$, where $s' = \pm$ labels the two split bands $\xi_{+,s'}$. This expression represents the difference between the contributions from these bands. Since band splitting implies $x_+ \neq x_-$, it follows that $K_0(x_+) \neq K_0(x_-)$, thereby guaranteeing a non-zero result for the summation. Consequently, for impurities on different surfaces, the two types of films can be unambiguously distinguished simply by observing the presence or absence of spin-frustrated terms.

Collectively, unlike the spin model constructed within the $m \neq 0$ framework in the subsection III-A—which fails to reflect the specific impact of intrinsic magnetism on the surface-state bands—the magnetic signatures extracted here can clearly delineate the precise modifications that intrinsic magnetism imposes on the surface-state bands of MnBi₂Te₄ films. These include corrections to the surface-state energy gap, the presence or absence of band splitting, and deformations of the Fermi surface. Therefore, the distinct RKKY signatures revealed here—such as the secondary kink, the transition in oscillation, and the emergence of spin-frustrated terms—can serve as a magnetic alternative for distinguishing between even- and odd-SL films. This approach provides a transport-independent means to resolve the experimental ambiguities encountered in prior transport-based studies [19, 24], where electrical measurements alone cannot reliably differentiate the AI phase (even-SL films) from the QAH phase (odd-SL films).

C. Identifying photoinduced phase transitions in even- and odd-SL regimes

To characterize the topological phase transition presented in Fig. 5, we examined the RKKY interaction for different impurity configurations. It is found that the magnetic interaction is most sensitive to the transition when impurities are placed on different surfaces. Additionally, in this section, we set the Fermi energy to zero, as this value best captures the behavior of the band gap closing and reopening.

As shown in Fig. 9, in even-SL ($\lambda = -$) films with impurities placed on different surfaces, the spin-frustrated term \mathcal{J}_f^x (or \mathcal{J}_f^y) defined in Eq. (20) provides a reliable magnetic signature. This signature not only identifies the occurrence of a topological transition but also reveals its dependence on circular polarization chirality η . Specifically, as the light pa-

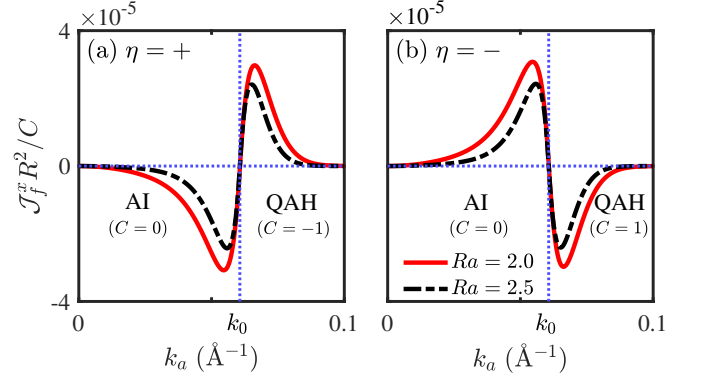


FIG. 9. The frustrated term \mathcal{J}_f^x as a function of k_a for even-SL MnBi₂Te₄ ($\lambda = -1$) under the (a) right-handed ($\eta = +$) and (b) left-handed ($\eta = -$) CPL, respectively. Impurities are placed on different surfaces with different distances ($Ra = 2.0, 2.5$). Here we set $\epsilon_F = 0$, $\Delta = 0.02$ eV, $v = 2.95$ eV·Å, $a = \Delta/v$, $\theta_R = \pi/4$ and $m = 0.025$ eV.

rameter k_a crosses the transition point $k_a = k_0$, \mathcal{J}_f^x undergoes a sign reversal—from negative to positive for right-handed ($\eta = +$) CPL, and conversely for left-handed ($\eta = -$) CPL—with its magnitude vanishing exactly at the transition point. These opposite sign reversals of \mathcal{J}_f^x correspond precisely to the η -dependent transitions (Fig. 5(a)), i.e., from the AI state ($C = 0$) to the QAH state with $C = -1$ for $\eta = +$ and $C = +1$ for $\eta = -$, respectively. This direct correspondence confirms the unique diagnostic power of \mathcal{J}_f^x .

The origin of this magnetic signature can be understood from Eqs. (19) and (21). For $\lambda = -$, \mathcal{J}_f^x is governed by the product of $g_0(\lambda = -)$ and $g(\lambda = -)$ (Eq. (21)). The function $g(\lambda = -)$ contributes a factor of η (Eq. (19)), which naturally introduces the circular polarization chirality dependence for \mathcal{J}_f^x . Meanwhile, $g_0(\lambda = -)$ contributes a factor of $k_a^2 - k_0^2$, which forces \mathcal{J}_f^x to change sign as k_a passes through k_0 . Therefore, the product of these two factors, $\eta(k_a^2 - k_0^2)$, directly and simultaneously explains the η -dependence and the sign reversal of \mathcal{J}_f^x at the phase transition point.

For photoinduced topological phase transitions in odd-SL ($\lambda = +$) films, the RKKY collinear components \mathcal{J}_{ii} ($i = x, y, z$) offer distinct magnetic signatures to identify the η -dependent transitions. This is exemplified by \mathcal{J}_{zz} in Fig. 10. Under right-handed ($\eta = +$) CPL, the gradual increase of the light parameter k_a produces two significant dips in \mathcal{J}_{zz} at the transition points k_1 and k_2 (Fig. 10(a)), serving as clear markers for the phase boundaries depicted in Fig. 5(b). The origin of these dips can be understood from the band evolution in Fig. 4. Around the transition point $k_a = k_1$, for instance, the band $E_{s,-}$ (red curve in Fig. 4) governs the gap closure and thus primarily contributes to \mathcal{J}_{zz} . As k_a approaches k_1 , the band $E_{s,-}$ moves toward the Fermi energy. This enhances the probability of electrons at its band edge being scattered between the two magnetic impurities, a process that peaks when the band touches the Fermi energy (i.e., the gap closes). Given that the RKKY interaction originates from electron scattering between impurities [63–67], this peak in the scattering probabil-

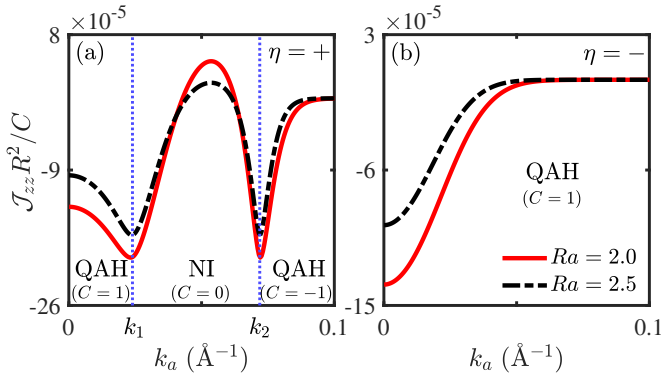


FIG. 10. The RKKY component J_{zz} as a function of k_a for odd-SL MnBi_2Te_4 ($\lambda = +$) under the (a) right-handed ($\eta = +$) and (b) left-handed ($\eta = -$) CPL, respectively. Impurities are placed on different surfaces with different distances ($Ra = 2.0, 2.5$). Other parameters are identical to those in Fig. 9.

ity naturally induces the strongest local magnetic interaction, manifesting as the observed dip in J_{zz} .

In stark contrast, under left-handed ($\eta = -$) CPL, the behavior is markedly different. As indicated in Fig. 10(b), the amplitude of J_{zz} monotonically decreases without any dip structure as the light parameter k_a increases. The absence of these characteristic dips indicates that no topological phase transition occurs under left-handed polarization, which is consistent with the constant topological index shown in Fig. 5(b). This behavior can be understood from the band evolution presented in Fig. 4(g-l): as k_a increases, all bands gradually shift away from the zero Fermi energy, which progressively suppresses the scattering processes of electrons between impurities—the very mechanism mediating the magnetic interaction—and thus ultimately leads to the monotonic decay of J_{zz} shown in Fig. 10(b).

IV. SUMMARY

We systematically investigated the RKKY interaction in MnBi_2Te_4 films. In the absence of external fields, several key magnetic signatures were identified. First, with axially arranged impurities, the RKKY spin model exhibits significantly stronger anisotropy in MnBi_2Te_4 than in nonmagnetic topological insulators, providing a clear distinguishing fea-

ture. Furthermore, we established three diagnostic signatures to differentiate between even-SL (AI state) and odd-SL (QAH state) films, which depend on the specific impurity configurations. The first two signatures, obtained with impurities on the same surface, are: (i) characteristic kinks in the Fermi-energy dependence of the RKKY amplitude (a single kink for even-SL vs. two for odd-SL); and (ii) distinct real-space oscillation patterns (a persistent single-period oscillation for even-SL vs. a transition to double-period oscillation for odd-SL). A third signature, observed with impurities on different surfaces, is the presence (odd-SL) or absence (even-SL) of spin-frustrated terms. All these signatures originate from the fundamental difference in band structures between even- and odd-SL films, a difference that is ultimately induced by the intrinsic magnetism. Finally, under off-resonant CPL, we extracted distinct magnetic responses from the spin-frustrated and collinear components, which provide signatures for topological phase transitions governed by polarization chirality and SL count.

Our work shows that measuring the RKKY interaction provides an effective alternative for characterizing band properties and phase transitions in MnBi_2Te_4 thin films, thereby offering a magnetic perspective to understand the influence of intrinsic magnetism on the surface-state band structure. The proposed scheme is feasible with existing techniques, such as spin-polarized scanning tunneling spectroscopy [68, 69], capable of detecting magnetization curves of individual atoms [69], or electron spin resonance techniques combined with optical detection methods [70].

ACKNOWLEDGMENTS

This work was supported by the National Natural Science Foundation of China (Grant Nos. 12104167, 12174121, 11904107, 11774100), by the Guangdong Basic and Applied Basic Research Foundation under Grant No. 2023B1515020050, by GDUPS (2017) and by Key Program for Guangdong NSF of China (Grant No. 2017B030311003).

DATA AVAILABILITY

The data that support the findings of this article are not publicly available. The data are available from the authors upon reasonable request.

[1] Y. Tokura, K. Yasuda, and A. Tsukazaki, Magnetic topological insulators, *Nat. Rev. Phys.* **1**, 126 (2019).

[2] M. Z. Hasan and C. L. Kane, Colloquium: Topological insulators, *Rev. Mod. Phys.* **82**, 3045 (2010).

[3] X.-L. Qi and S.-C. Zhang, Topological insulators and superconductors, *Rev. Mod. Phys.* **83**, 1057 (2011).

[4] P. Li, J. Yu, Y. Wang, and W. Luo, Electronic structure and topological phases of the magnetic layered materials MnBi_2Te_4 , MnBi_2Se_4 , and MnSb_2Te_4 , *Phys. Rev. B* **103**, 155118 (2021).

[5] F. Lüpke, A. D. Pham, Y.-F. Zhao, L.-J. Zhou, W. Lu, E. Briggs, J. Bernholc, M. Kolmer, J. Teeter, W. Ko, C.-Z. Chang, P. Ganesh, and A.-P. Li, Local manifestations of thickness-dependent topology and edge states in the topological magnet MnBi_2Te_4 , *Phys. Rev. B* **105**, 035423 (2022).

[6] F. D. M. Haldane, Model for a quantum hall effect without landau levels: Condensed-matter realization of the "parity anomaly", *Phys. Rev. Lett.* **61**, 2015 (1988).

[7] R. Yu, W. Zhang, H.-J. Zhang, S.-C. Zhang, X. Dai, and Z. Fang, Quantized anomalous Hall effect in magnetic topological insulators, *Science* **329**, 61 (2010).

[8] C.-Z. Chang, J. Zhang, X. Feng, J. Shen, Z. Zhang, M. Guo, K. Li, Y. Ou, P. Wei, L.-L. Wang, Z.-Q. Ji, Y. Feng, S. Ji, X. Chen, J. Jia, X. Dai, Z. Fang, S.-C. Zhang, K. He, Y. Wang, L. Lu, X.-C. Ma, and Q.-K. Xue, Experimental observation of the quantum anomalous Hall effect in a magnetic topological insulator, *Science* **340**, 167 (2013).

[9] X.-L. Qi, T. L. Hughes, and S.-C. Zhang, Topological field theory of time-reversal invariant insulators, *Phys. Rev. B* **78**, 195424 (2008).

[10] A. M. Essin, J. E. Moore, and D. Vanderbilt, Magnetoelectric polarizability and axion electrodynamics in crystalline insulators, *Phys. Rev. Lett.* **102**, 146805 (2009).

[11] R. S. K. Mong, A. M. Essin, and J. E. Moore, Antiferromagnetic topological insulators, *Phys. Rev. B* **81**, 245209 (2010).

[12] A. Das, Y. Ronen, Y. Most, Y. Oreg, M. Heiblum, and H. Shtrikman, Zero-bias peaks and splitting in an Al-InAs nanowire topological superconductor as a signature of majorana fermions, *Nat. Phys.* **8**, 887 (2012).

[13] J. G. Checkelsky, R. Yoshimi, A. Tsukazaki, K. S. Takahashi, Y. Kozuka, J. Falson, M. Kawasaki, and Y. Tokura, Trajectory of the anomalous Hall effect towards the quantized state in a ferromagnetic topological insulator, *Nat. Phys.* **10**, 731 (2014).

[14] C.-Z. Chang, W. Zhao, D. Y. Kim, H. Zhang, B. A. Assaf, D. Heiman, S.-C. Zhang, C. Liu, M. H. W. Chan, and J. S. Moodera, High-precision realization of robust quantum anomalous Hall state in a hard ferromagnetic topological insulator, *Nat. Mater.* **14**, 473 (2015).

[15] M. M. Otkov, I. I. Klimovskikh, H. Bentmann, D. Estyulin, A. Zeugner, Z. S. Aliev, S. Gaß, A. U. B. Wolter, A. V. Koroleva, A. M. Shikin, M. Blanco-Rey, M. Hoffmann, I. P. Rusinov, A. Y. Vyazovskaya, S. V. Eremeev, Y. M. Koroteev, V. M. Kuznetsov, F. Freyse, J. Sánchez-Barriga, I. R. Amiraslanov, M. B. Babanly, N. T. Mamedov, N. A. Abdullayev, V. N. Zverev, A. Alfonsov, V. Kataev, B. Büchner, E. F. Schwier, S. Kumar, A. Kimura, L. Petaccia, G. Di Santo, R. C. Vidal, S. Schatz, K. Kißner, M. Ünzelmann, C. H. Min, S. Moser, T. R. F. Peixoto, F. Reinert, A. Ernst, P. M. Echenique, A. Isaeva, and E. V. Chulkov, Prediction and observation of an antiferromagnetic topological insulator, *Nature* **576**, 416 (2019).

[16] Y. Gong, J. Guo, J. Li, K. Zhu, M. Liao, X. Liu, Q. Zhang, L. Gu, L. Tang, X. Feng, D. Zhang, W. Li, C. Song, L. Wang, P. Yu, X. Chen, Y. Wang, H. Yao, W. Duan, Y. Xu, S.-C. Zhang, X. Ma, Q.-K. Xue, and K. He, Experimental realization of an intrinsic magnetic topological insulator, *Chin. Phys. Lett.* **36**, 076801 (2019).

[17] D. Zhang, M. Shi, T. Zhu, D. Xing, H. Zhang, and J. Wang, Topological axion states in the magnetic insulator MnBi_2Te_4 with the quantized magnetoelectric effect, *Phys. Rev. Lett.* **122**, 206401 (2019).

[18] M. M. Otkov, I. P. Rusinov, M. Blanco-Rey, M. Hoffmann, A. Y. Vyazovskaya, S. V. Eremeev, A. Ernst, P. M. Echenique, A. Arnau, and E. V. Chulkov, Unique thickness-dependent properties of the van der Waals interlayer antiferromagnet MnBi_2Te_4 films, *Phys. Rev. Lett.* **122**, 107202 (2019).

[19] C. Liu, Y. Wang, H. Li, Y. Wu, Y. Li, J. Li, K. He, Y. Xu, J. Zhang, and Y. Wang, Robust axion insulator and chern insulator phases in a two-dimensional antiferromagnetic topological insulator, *Nat. Mater.* **19**, 522 (2020).

[20] K. Nomura and N. Nagaosa, Surface-quantized anomalous Hall current and the magnetoelectric effect in magnetically disordered topological insulators, *Phys. Rev. Lett.* **106**, 166802 (2011).

[21] J. Wang, B. Lian, X.-L. Qi, and S.-C. Zhang, Quantized topological magnetoelectric effect of the zero-plateau quantum anomalous Hall state, *Phys. Rev. B* **92**, 081107 (2015).

[22] N. Varnava and D. Vanderbilt, Surfaces of axion insulators, *Phys. Rev. B* **98**, 245117 (2018).

[23] Y. Deng, Y. Yu, M. Z. Shi, Z. Guo, Z. Xu, J. Wang, X. H. Chen, and Y. Zhang, Quantum anomalous Hall effect in intrinsic magnetic topological insulator MnBi_2Te_4 , *Science* **367**, 895 (2020).

[24] D. Ovchinnikov, X. Huang, Z. Lin, Z. Fei, J. Cai, T. Song, M. He, Q. Jiang, C. Wang, H. Li, Y. Wang, Y. Wu, D. Xiao, J. H. Chu, J. Yan, C. Z. Chang, Y. T. Cui, and X. Xu, Intertwined topological and magnetic orders in atomically thin chern insulator MnBi_2Te_4 , *Nano Lett.* **21**, 2544 (2021).

[25] C.-Z. Chang, C.-X. Liu, and A. H. MacDonald, Colloquium: Quantum anomalous Hall effect, *Rev. Mod. Phys.* **95**, 011002 (2023).

[26] T. Zhu, H. Wang, and H. Zhang, Floquet engineering of magnetic topological insulator MnBi_2Te_4 films, *Phys. Rev. B* **107**, 085151 (2023).

[27] C. Zhou and J. Zhou, Light-Induced Topological Phase Transition with Tunable Layer Hall Effect in Axion Antiferromagnets, *Nano Lett.* **24**, 7311 (2024).

[28] J.-J. Zhu, D.-X. Yao, S.-C. Zhang, and K. Chang, Electrically controllable surface magnetism on the surface of topological insulators, *Phys. Rev. Lett.* **106**, 097201 (2011).

[29] M. Zare, F. Parhizgar, and R. Asgari, Topological phase and edge states dependence of the RKKY interaction in zigzag silicene nanoribbon, *Phys. Rev. B* **94**, 045443 (2016).

[30] S.-X. Wang, H.-R. Chang, and J. Zhou, RKKY interaction in three-dimensional electron gases with linear spin-orbit coupling, *Phys. Rev. B* **96**, 115204 (2017).

[31] S. F. Islam, P. Dutta, A. M. Jayannavar, and A. Saha, Probing decoupled edge states in a zigzag phosphorene nanoribbon via RKKY exchange interaction, *Phys. Rev. B* **97**, 235424 (2018).

[32] V. Kaladzhyan, A. A. Zyuzin, and P. Simon, RKKY interaction on the surface of three-dimensional Dirac semimetals, *Phys. Rev. B* **99**, 165302 (2019).

[33] H.-J. Duan, Y.-J. Wu, M.-X. Deng, R.-Q. Wang, and M. Yang, Indirect magnetic signals in Weyl semimetals mediated by a single fermi arc, *Phys. Rev. B* **107**, 165147 (2023).

[34] H.-J. Duan, S.-H. Zheng, Y.-Y. Yang, C.-Y. Zhu, M.-X. Deng, M. Yang, and R.-Q. Wang, Anisotropic RKKY interactions in nodal-line semimetals, *Phys. Rev. B* **102**, 165110 (2020).

[35] H.-R. Chang, J. Zhou, S.-X. Wang, W.-Y. Shan, and D. Xiao, RKKY interaction of magnetic impurities in Dirac and Weyl semimetals, *Phys. Rev. B* **92**, 241103 (2015).

[36] M. V. Hosseini and M. Askari, Ruderman-Kittel-Kasuya-Yosida interaction in Weyl semimetals, *Phys. Rev. B* **92**, 224435 (2015).

[37] H.-J. Duan, S.-H. Zheng, P.-H. Fu, R.-Q. Wang, J.-F. Liu, G.-H. Wang, and M. Yang, Indirect magnetic interaction mediated by Fermi arc and boundary reflection near Weyl semimetal surface, *New J. Phys.* **20**, 103008 (2018).

[38] G. C. Paul, S. F. Islam, P. Dutta, and A. Saha, Signatures of interfacial topological chiral modes via RKKY exchange interaction in Dirac and Weyl systems, *Phys. Rev. B* **103**, 115306 (2021).

[39] G. C. Paul, S. F. Islam, and A. Saha, Fingerprints of tilted Dirac cones on the RKKY exchange interaction in 8-Pmmn borophene, *Phys. Rev. B* **99**, 155418 (2019).

[40] H.-J. Duan, S.-H. Zheng, R.-Q. Wang, M.-X. Deng, and M. Yang, Signature of indirect magnetic interaction in

the crossover from type-I to type-II Weyl semimetals, *Phys. Rev. B* **99**, 165111 (2019).

[41] H.-J. Duan, Y.-J. Wu, Y.-Y. Yang, S.-H. Zheng, C.-Y. Zhu, M.-X. Deng, M. Yang, and R.-Q. Wang, The prolonged decay of RKKY interactions by interplay of relativistic and non-relativistic electrons in semi-Dirac semimetals, *New J. Phys.* **24**, 033029 (2022).

[42] M. Ke, M. M. Asmar, and W.-K. Tse, Nonequilibrium RKKY interaction in irradiated graphene, *Phys. Rev. Res.* **2**, 033228 (2020).

[43] M. M. Asmar and W.-K. Tse, Floquet control of indirect exchange interaction in periodically driven two-dimensional electron systems, *New J. Phys.* **23**, 123031 (2021).

[44] M. Yarmohammadi, M. Bukov, and M. H. Kolodrubetz, Non-collinear twisted RKKY interaction on the optically driven SnTe(001) surface, *Phys. Rev. B* **107**, 054439 (2023).

[45] Y.-L. Lee, Magnetic impurities in an altermagnetic metal, *Eur. Phys. J. B* **98**, 43 (2025).

[46] M. Amundsen, A. Brataas, and J. Linder, RKKY interaction in Rashba altermagnets, *Phys. Rev. B* **110**, 054427 (2024).

[47] M. Yarmohammadi, U. Zülicke, J. Berakdar, J. Linder, and J. K. Freericks, Anisotropic light-tailored RKKY interaction in two-dimensional *d*-wave altermagnets, *Phys. Rev. B* **111**, 224412 (2025).

[48] M. Zhou, H.-R. Chang, L. Yang, and L. Liang, Weyl-mediated Ruderman-Kittel-Kasuya-Yosida interaction revisited: Imaginary-time formalism and finite temperature effects, *Phys. Rev. B* **112**, 054449 (2025).

[49] M. Yarmohammadi, S. R. Koshkaki, J. Berakdar, M. Bukov, and M. H. Kolodrubetz, Probing topological phases in a perturbed Kane-Mele model via RKKY interaction: Application to monolayer jacutingaite Pt_2HgSe_3 , *Phys. Rev. B* **111**, 014440 (2025).

[50] M. Shiranzaei, J. Fransson, H. Cheraghchi, and F. Parhizgar, Nonlinear spin susceptibility in topological insulators, *Phys. Rev. B* **97**, 180402 (2018).

[51] T. V. Trevisan, P. V. Arribi, O. Heinonen, R.-J. Slager, and P. P. Orth, Bicircular Light Floquet Engineering of Magnetic Symmetry and Topology and Its Application to the Dirac Semimetal Cd_3As_2 , *Phys. Rev. Lett.* **128**, 066602 (2022).

[52] T. Mikami, S. Kitamura, K. Yasuda, N. Tsuji, T. Oka, and H. Aoki, Brillouin-Wigner theory for high-frequency expansion in periodically driven systems: Application to Floquet topological insulators, *Phys. Rev. B* **93**, 144307 (2016).

[53] Z. Yan and Z. Wang, Tunable Weyl Points in Periodically Driven Nodal Line Semimetals, *Phys. Rev. Lett.* **117**, 087402 (2016).

[54] D. Xiao, M.-C. Chang, and Q. Niu, Berry phase effects on electronic properties, *Rev. Mod. Phys.* **82**, 1959 (2010).

[55] M. A. Ruderman and C. Kittel, Indirect exchange coupling of nuclear magnetic moments by conduction electrons, *Phys. Rev.* **96**, 99 (1954).

[56] T. Kasuya, A Theory of Metallic Ferro- and Antiferromagnetism on Zener's Model, *Prog. Theor. Phys.* **16**, 45 (1956).

[57] K. Yosida, Magnetic Properties of Cu-Mn Alloys, *Phys. Rev.* **106**, 893 (1957).

[58] D. C. Mattis, *The Theory of Magnetism Made Simple: An Introduction to Physical Concepts and to Some Useful Mathematical Methods* (World Scientific, Singapore, 2006).

[59] M. Shiranzaei, H. Cheraghchi, and F. Parhizgar, Effect of the Rashba splitting on the RKKY interaction in topological-insulator thin films, *Phys. Rev. B* **96**, 024413 (2017).

[60] M. M. Asmar and W.-K. Tse, Interlayer RKKY coupling in bulk Rashba semiconductors under topological phase transition, *Phys. Rev. B* **100**, 014410 (2019).

[61] Y.-J. Wu, Q.-Y. Xiong, H.-J. Duan, J.-Y. Ba, M.-X. Deng, and R.-Q. Wang, Interlayer RKKY interaction in ferromagnet/tilted Weyl semimetal/ferromagnet trilayer system, *Phys. Rev. B* **106**, 195130 (2022).

[62] H.-J. Duan, Y.-J. Wu, M.-X. Deng, R.-Q. Wang, and M. Yang, Indirect magnetic signals in Weyl semimetals mediated by a single Fermi arc, *Phys. Rev. B* **107**, 165147 (2023).

[63] S.-H. Zhang, J.-J. Zhu, W. Yang, and K. Chang, Focusing RKKY interaction by graphene P-N junction, *2D Mater.* **4**, 035005 (2017).

[64] S.-H. Zhang, J.-J. Zhu, W. Yang, and K. Chang, Selective generation and amplification of RKKY interactions by a *p-n* interface, *Phys. Rev. B* **99**, 195456 (2019).

[65] S.-H. Zhang and W. Yang, Anomalous caustics and Veselago focusing in 8-Pmmn borophene *p-n* junctions with arbitrary junction directions, *New J. Phys.* **21**, 103052 (2019).

[66] S.-H. Zhang, D.-F. Shao, and W. Yang, Velocity-determined anisotropic behaviors of RKKY interaction in 8-pmmn borophene, *J. Magn. Magn. Mater.* **491**, 165631 (2019).

[67] S.-H. Zhang, J. Yang, D.-F. Shao, W. Yang, and K. Chang, Geometric wavefront dislocations of RKKY interaction in graphene, *Phys. Rev. B* **104**, 245405 (2021).

[68] L. Zhou, J. Wiebe, S. Lounis, E. Vedmedenko, F. Meier, S. Blügel, P. H. Dederichs, and R. Wiesendanger, Strength and directionality of surface Ruderman-Kittel-Kasuya-Yosida interaction mapped on the atomic scale, *Nat. Phys.* **6**, 187 (2010).

[69] F. Meier, L. Zhou, J. Wiebe, and R. Wiesendanger, Revealing Magnetic Interactions from Single-Atom Magnetization Curves, *Science* **320**, 82 (2008).

[70] C. Laplane, E. Zambrini Cruzeiro, F. Fröwis, P. Goldner, and M. Afzelius, High-Precision Measurement of the Dzyaloshinsky-Moriya Interaction between Two Rare-Earth Ions in a Solid, *Phys. Rev. Lett.* **117**, 037203 (2016).